

A Deep Radio Survey of Abell 2125. I. Radio, Optical, and
Near-Infrared Observations

Frazer N. Owen – National Radio Astronomy Observatory, Socorro, NM

W. C. Keel – University of Alabama

M. J. Ledlow – Gemini Observatory Southern Operations Center, Chile

G. E. Morrison – National Optical Astronomy Observatory Tucson, AZ

R. A. Windhorst – Arizona State University

Deposited 09/24/2018

Citation of published version:

Owen, F., Keel, W., Ledlow, M., Morrison, G., Windhorst, R. (2005): A Deep Radio Survey of Abell 2125. I. Radio, Optical, and Near-Infrared Observations. *The Astronomical Journal*, 129(1). DOI: [10.1086/426322](https://doi.org/10.1086/426322)

A DEEP RADIO SURVEY OF ABELL 2125. I. RADIO, OPTICAL, AND NEAR-INFRARED OBSERVATIONS

FRAZER N. OWEN,^{1,2} W. C. KEEL,^{2,3} M. J. LEDLOW,^{2,4,5} G. E. MORRISON,^{2,6} AND R. A. WINDHORST^{2,7}

Received 2004 July 1; accepted 2004 September 15

ABSTRACT

We present a description of deep radio, optical, and near-IR observations taken with the VLA, the KPNO 2 m telescope, and the KPNO 4 m telescope of the region containing the rich cluster of galaxies Abell 2125. The reduction of each data set is described. A catalog of radio sources apparently not associated with members of A2125 and the associated *R*-band magnitudes is presented.

Key words: cosmology: observations — galaxies: clusters: individual (Abell 2125) — galaxies: evolution — galaxies: starburst — infrared: galaxies

Online material: machine-readable table

1. INTRODUCTION

Deep radio observations offer one of the important windows on the evolution of star formation and black hole–related activity as a function of cosmological epoch. Radio, optical/near-IR, far-IR, and X-ray data taken together have the potential eventually to give us a well-constrained picture of our history. Each window, by itself, has serious weaknesses. The optical/near-IR window is the best studied and provides the most direct view. However, it suffers from uncertainties due to dust obscuration, a fundamental part of star formation. Far-infrared (FIR) observations give us a signal from the dust but leave uncertain the origin of the heating of the dust and fail to see into the heart of the active galactic nuclei (AGNs) or star-forming regions. In X-rays and radio, we can see behind the dust, but we are measuring secondary emission, which is not easy to relate physically to the black hole physics or star formation rate (SFR). Thus, we need a combination of all this information to deduce the full picture.

Below $L_{20\text{ cm}} \sim 10^{23} \text{ W Hz}^{-1}$, one can show that locally the radio luminosity function is dominated by synchrotron emission related to star formation–driven processes (e.g., Condon 1992). Above this luminosity most sources are twin-jet, black hole–driven sources. Below the $10^{23} \text{ W Hz}^{-1}$ break point, the sources are mostly found in spiral galaxies rather than elliptical galaxies, and the radio and FIR luminosities correlate very well (see, e.g., Yun et al. 2001). Through the radio-FIR correlation, one can estimate the SFR for the radio alone and can use the

ratio of radio to submillimeter emission to constrain the redshift (assuming the empirical radio-FIR relation continues to hold at any redshift; Carilli & Yun 1999). Thus, deep radio observations with limiting flux densities $\ll 1$ mJy offer a way to study star formation in the distant universe.

However, there are a lot of assumptions in the previous paragraph. What one really needs are deep data in all four windows to understand the picture. Where we have such information new puzzles arise. For example, SCUBA submillimeter sources are usually associated with faint radio sources. Using the superior radio positions, one can make faint optical identifications and try to measure redshifts. Often when an optical redshift can be obtained, one finds an AGN spectrum (e.g., Ledlow et al. 2002). Even so, the redshift estimated from the Carilli-Yun relation agrees with the measured value. Perhaps this is a coincidence, but it might suggest that bright black hole–driven AGNs are part of the star formation process in galaxies.

We are interested in both the very distant star formation/AGN history and the same phenomena in intermediate-distance rich clusters ($0.2 \lesssim z \lesssim 0.4$). A deep radio survey in the direction of such a cluster can be used for both purposes. This paper reports deep radio observations in the direction of A2125. Future papers will report the combination of these data with observations in other bands to study both problems.

We began studying the A2125 field with medium-deep 20 cm VLA C-configuration observations (Dwarakanath & Owen 1999; Owen et al. 1999). We compared A2125 (a richness class 4, blue cluster at $z \sim 0.25$) with A2645 (an apparently similar cluster at the same redshift but with much redder galaxies). We found a much higher detection rate of radio galaxies (27 vs. 4) in A2125. The detection rate in A2645 is consistent with a normal AGN population in a lower redshift cluster. The A2125 excess population occurs entirely with luminosities below $L_{20\text{ cm}} \sim 10^{23} \text{ W Hz}^{-1}$ and thus seems consistent with a star-forming population. However, only a small fraction of the excess population have optical spectra consistent with enough star formation activity to explain the population entirely that way. Either the star-forming activity is very well hidden in the majority of the low radio luminosity sample, or some other explanation is necessary for the radio activity.

One possible clue is that A2125 does not appear to be a typical very rich cluster when examined in more detail in the optical and X-ray bands. Optically, the cluster consists of a

¹ National Radio Astronomy Observatory, P.O. Box O, Socorro, NM 87801; fowen@nrao.edu. The National Radio Astronomy Observatory is a facility of the National Science Foundation (NSF) operated under cooperative agreement by Associated Universities, Inc.

² Visiting Astronomer, Kitt Peak National Observatory (KPNO), National Optical Astronomy Observatory, which is operated by the Association of Universities for Research in Astronomy, Inc., under cooperative agreement with the NSF.

³ Department of Physics and Astronomy, University of Alabama, Tuscaloosa, AL 35487-0324.

⁴ Gemini Observatory Southern Operations Center, Casilla 603, La Serena, Chile.

⁵ Deceased 2004 June 5. We will miss his cheerfulness, unflinching good sense, and scientific industry.

⁶ National Optical Astronomy Observatory, 950 North Cherry Avenue, Tucson, AZ 85719.

⁷ Department of Physics and Astronomy, Arizona State University, Tempe, AZ 85287-1504.

central concentration together with an extension to the southwest extending at least 2 Mpc. X-ray observations (Wang et al. 1997) show the same pattern and imply that the total X-ray luminosity is low for such a rich cluster. Much of the excess X-ray population is contained in the southwest extension, not the cluster core. Thus, perhaps these unusual properties have something to do with the radio excess.

To study the cluster further, we have made much deeper radio observations at higher resolution using all four VLA configurations. The deep radio data have also motivated deep optical and near-infrared (NIR) imaging, optical spectroscopy (Miller et al. 2004), deep millimeter and submillimeter observations (Eales et al. 2003), and a deep *Chandra* exposure (Wang et al. 2004). In some cases, these ancillary observations were not motivated by the cluster but by the possibility of studying the background sample (e.g., the submillimeter survey). In this paper we document the techniques used in reducing the radio and optical imaging data for this field. We also report the radio data and *R*-band optical identifications for these data. A companion paper (Owen et al. 2005b, hereafter Paper II) contains the results for the radio sources confirmed to be associated with cluster members.

2. OBSERVATIONS, REDUCTION, AND CATALOGING

Observations were made with the VLA for 3.5 hr in the 1997 B configuration and for 27.5 hr in the 1998 A configuration. Since the total time is dominated by the A configuration, the final image for analysis had a resolution of about $1''.5$. The data were all taken in spectral line mode 4, which provides seven 3.125 MHz channels in each of two intermediate frequencies (IFs; centered at 1365 and 1435 MHz) and each of two polarizations. Integration times of 5 s were used in the A and B configurations. The integration times and channel bandwidths were chosen to minimize tangential and radial smearing of the images away from the field center. It would be better to use narrower channel widths and shorter integration times to eliminate such effects totally, but the mode we picked seems to be the best compromise given the current VLA correlator and data-handling system. Another important consideration for deep VLA work at 20 cm with the present system is that the system temperature increases as a function of zenith distance because of increased ground pickup. For this reason, almost all the observations were scheduled within 3 hr of source transit to minimize this effect.

2.1. Calibration and Editing

All radio reductions use the AIPS package. Since the total bandwidth is relatively large for a spectral line experiment, for each daily observation we first split a bright point-source calibrator from the raw database and applied a phase self-calibration. We then used this otherwise uncalibrated source to calculate a bandpass correction before we proceeded with the rest of the regular continuum calibration. Regular continuum calibration then continued, using the bandpass calibration to flatten the spectral response and thus avoid the effects of the raw, sloping spectral response. Calibration was made in the standard way to the Baars flux density scale using 3C 286 as the flux calibrator. The weights associated with each integration were also calibrated as a function of observed system temperature and calibrated as part of the standard AIPS processing. The calibrated data set was first clipped using the AIPS program CLIP well above the total flux density found in the field from lower resolution observations, in order to remove a few high points before beginning the self-calibration process.

2.2. Imaging and Self-Calibration

The entire primary beam was then imaged using the AIPS task IMAGR and the three-dimensional, multifacet options. Besides 37 facets, each with 1000×1000 points, to describe the primary beam, another 37 facets, each with 500×500 points, were centered on all the remaining detectable sources outside of the central region. This is particularly important at 20 cm, since the feed is a compromise, using a lens to illuminate the primary reflector. This feed causes both a higher system temperature as a function of elevation and a high first-sidelobe response for the primary beam. The result of this is that many outlying sources are detected in the first sidelobe, as well as a few further out that need to be removed. This was accomplished using the 37 outlying facets. After initial imaging, each detected source had a tight clean box placed around it to limit cleaning to real features. This procedure allows each image to be cleaned down to the 1σ level and permits the resulting clean components to be used in the self-calibration process. This process also eliminates almost all the clean bias and does not artificially reduce the noise on the image, as happens when one does not use boxes.

The images were self-calibrated, first just in phase and later in both amplitude and phase, using the AIPS task CALIB. However, these images were limited by the pointing changes on outlying bright sources. This is primarily due to the fact that the two circular polarizations have different pointing centers (i.e., beam squint) on the VLA because of the slightly off-axis location of the feeds. This, combined with the altitude-azimuth geometry of the telescopes, causes the effective gain on a source far off-axis to vary with hour angle. In addition, the slightly different frequencies of the two IFs causes a slightly different primary beam size, and thus a source far from the field center has a higher gain at the lower frequency. As a final step to correct approximately for these two effects, the *u-v* data sets were split into their separate IFs (two), polarizations (two), and hour-angle ranges (four). They were then imaged and self-calibrated separately. Finally, the eight images of each facet were combined, weighting each by $1/\text{rms}^2$ to form an optimum final image.

The final images typically had an rms noise before correction for the primary beam of $6.5 \mu\text{Jy}$, somewhat larger near very bright sources. The final full-resolution images had a Gaussian clean beam with a FWHM of $1''.60 \times 1''.52$ at a position angle of $87^\circ.9$.

2.3. Cataloging

The inner $25' \times 25'$ region of the final image was chosen for cataloging and further study. Beyond this region, the losses due to the bandwidth smearing and the primary-beam attenuation were judged to be too large for useful analysis. The AIPS program SAD was used for forming the initial source lists down to peak flux densities of $20 \mu\text{Jy beam}^{-1}$. The residual images from SAD were then searched to find any remaining sources missed by SAD. Lower resolution images with $3'' \times 3''$ and $5'' \times 5''$ were also constructed in order to search for lower surface brightness sources and to check the fitted angular sizes for possible larger components than were detected in the full-resolution images.

The full list of detected sources was then inspected and fitted manually using JMFIT. The parameter BWSMEAR was used to take into account the finite bandwidth of the individual 3.125 MHz channels used for the observing. Without using this parameter, bandwidth smearing makes sources appear to be the size of the fractional bandwidth times the distance from the field center, elongated radially from the phase pointing center. This

results in typical apparent source sizes of $\sim 2''$ over the field analyzed and may account for some previous studies with the VLA that found that typical size for sources in their samples. Sources that were found by JMFIT to have zero as the minimum size of the major axis were assumed to be unresolved. For such sources, the maximum allowed size for the source on either axis was adopted as the upper limit to the angular extent. For unresolved sources, simulations have shown that the fitted peak flux density for the unconstrained Gaussian functions fitted with JMFIT is the best estimate to the total flux density (E. Greisen 2002, private communication). Thus, for sources with only upper limits to their size this estimate of the total flux density is used. For significantly resolved sources, the total fitted flux density is adopted. Errors in the flux density and position were calculated using the formalism of Condon et al. (1998).

The local noise was estimated locally using the AIPS program RMSD in a $100 \text{ pixel} \times 100 \text{ pixel}$ region centered on each pixel. This calculation was made on a mosaicked image of the entire $25' \times 25'$ of the central field. The resulting noise image was then corrected for the primary-beam attenuation, the bandwidth smearing, and approximately for time averaging to produce a local noise image for the survey. This result was then used to pick a source that had 5σ peaks in excess of the local noise on the full-resolution image.

2.4. Optical Imaging

Optical and NIR images for the field were obtained of the same field in 2000 June, using MOSAIC on the KPNO 4 m telescope and SQUID on the KPNO 2.1 m telescope. With MOSAIC, images were obtained in eight bands: *U*, *B*, *V*, *R*, *I*, BATC 8010A, BATC 9170A, and WR CIII. The BATC filters (Fan et al. 1996; Xia et al. 2002) are special medium-bandwidth filters ($\sim 250 \text{ \AA}$) designed to fit in the clearest optical windows in the red. WR CIII is a narrowband filter centered at 4253 \AA with a FWHM of 52 \AA ; we used it to isolate [O II] at the redshift of A2125. Total exposure times were *U*, 6 hr; *B*, 2 hr; *V*, 2 hr; *R*, 4 hr; *I*, 1 hr; 8010A, 2 hr; 9170A, 2 hr; and WR CIII, 3.6 hr. The pointings were dithered to five separate pointings near the field center and then flattened and combined using the standard IRAF MOSAIC software as described by Valdes (2002). The standards of Landolt (1992) were used to set the magnitude scales on the *UBVRI* images. The US Naval Observatory catalog of objects from the Palomar Sky Survey was used to set the astrometry on each final image. Each final image has a pixel size of $0''.26$ and is 8700×8800 pixels.

2.5. Near-IR Imaging

The SQUID images were taken simultaneously in *J*, *H*, and *K*. Each image has a usable field of $\sim 5'.2 \times 5'.2$. Observations were obtained with SQUID over a 3×3 grid with $35''$ overlap across adjacent fields, yielding a mosaicked field of view of $16'.5$. The mosaic consisted of 24 co-adds of 10 s at each grid pointing. We applied random offsets between successive iterations of the mosaic. The total useful exposure time on the field was about 7 hr. More integration time was spent on the central field and the field to the east of the center than on the other seven pointings.

Since mosaicking a large area of sky with SQUID is not a standard observational mode, we summarize our data reduction method here. We first subtracted off a stacked dark exposure from all frames. For the sky subtraction, we created a list of exposures over a ± 30 minute window. Each frame was inspected, and those with bright stars or higher than average background were removed. The dark-subtracted sky frame was then subtracted from all object frames in that time window. A

master flat field was created from all suitable exposures over the night and combined with σ -clipping and mode scaling. After flat-fielding, we removed any large-scale residual sky gradients by subtracting a median-filtered version of each frame. Next, each frame was corrected for geometric distortion. The distortion map was determined separately for each filter on the basis of a cross-correlation of objects with our deep *R*-band frame, which had been previously regridded to a proper world coordinate system (distortions removed). Finally, we applied a bad-pixel mask to each frame that set bad regions to a very large positive number (100,000) to facilitate threshold clipping during co-addition. Registering and stacking the data was accomplished by creating a zero-level image larger than the full field of the 3×3 grid (1800 pixels) and pasting each exposure into this image template. We used our *R*-band image (same image scale) as the reference image for determining pixel shifts. After measuring the shifts for each of the nine frames in the grid, the frames were shifted and co-added with inverse-variance weighting and an upper threshold value set to clip off the bad regions set by the masking.

3. RESULTS

Observations were taken of this field to study both the cluster and noncluster radio populations in the field of A2125. The cluster members were isolated using spectroscopic redshifts as reported in Miller et al. (2004) and are discussed in detail in Paper II. The remaining radio-detected objects are believed to be predominantly background sources. First, most have optical identifications much too faint to be cluster members and/or have spectroscopic redshifts outside the cluster limits. Second, as reported in Owen et al. (2005a), our photometric redshift estimates or limits for very faint objects based on the implied absolute magnitudes for almost all the remaining objects are consistent with much higher redshifts than that of A2125 ($z = 0.247$). These sources and their parameters are listed below. We will supply FITS images of the radio and optical images on request.

3.1. Radio Catalog

In Table 1, we give the final source list and parameters from the fits. Column (1) contains the source name. The first two digits are the facet number, and the last three are a sequence number. Columns (2) and (3) contain the radio right ascension and declination, along with the estimated error. In column (4) we give the distance from the pointing center (R.A. = $15^{\text{h}}41^{\text{m}}14^{\text{s}}.00$, decl. = $66^{\circ}15'00''.0$) in arcminutes. Column (5) contains the observed (uncorrected) peak flux density from the map in microjanskys per beam. In column (6) we list the corrected total flux density and the estimated error. In column (7), we give the best-fitting size in arcseconds. If a two-dimensional Gaussian was the best fit, we give the major- and minor-axis size (FWHM) and the position angle. Upper limits are given for sources that were unresolved. Sources with sizes only were estimated directly from the maps using the AIPS task TVSTAT. Column (8) contains the *R*-band optical magnitude in an aperture of radius $2''$. Finally, column (9) gives the optical/NIR identification status: “i” indicates an identification in at least one of the 10 observed bands, “b” indicates a blank field, and “c” indicates an optical field that is too confused to be sure of the identification. For the full sample of 357 radio sources, 82% had a optical identification, 10% were confused, and 8% were blank and not confused.

3.2. Optical Identifications

Most of the sources in the radio catalog have clear identifications in the *R*-band image. For sources with apparent IDs

TABLE 1
NON-CLUSTER MEMBER RADIO SOURCES

Name (1)	R.A. (J2000.0) (2)	Decl. (J2000.0) (3)	Distance (arcmin) (4)	Peak ($\mu\text{Jy beam}^{-1}$) (5)	Total (μJy) (6)	Size (arcsec) (7)	R Magnitude (8)	ID (9)
18002.....	15 39 10.81 (0.05)	66 14 58.3 (0.3)	12.4	69.9	157.6 (16)	<1.7	22.44	i
11001.....	15 39 11.21 (0.06)	66 19 45.9 (0.4)	13.2	70.0	193.9 (28)	1.6×0 , p.a. = 118°	0.00	b
11002.....	15 39 12.88 (0.07)	66 25 10.1 (0.4)	15.8	38.8	131.2 (24)	<1.2	23.48	i
18003.....	15 39 13.42 (0.07)	66 12 15.7 (0.4)	12.5	63.9	179.6 (28)	1.6×0.2 , p.a. = 71°	24.42	i
11003.....	15 39 14.08 (0.08)	66 22 20.2 (0.5)	14.1	46.8	169.4 (37)	1.9×0.3 , p.a. = 108°	0.00	b

NOTES.—Table 1 is presented in its entirety in the electronic edition of the *Astronomical Journal*. A portion is shown here for guidance regarding its form and content. Units of right ascension are hours, minutes, and seconds, and units of declination are degrees, arcminutes, and arcseconds.

within $1''$ of the radio position, the mean radio-optical offset is $-0''.035$ in right ascension ($-0''.2$) and $-0''.1$ in declination. After correcting for these offsets, the mean radio-optical separation is $0''.3$. In Figure 1, we show a histogram of the total radio-optical offset. Clearly, most of the sources agree within a few tenths of an arcsecond. However, both some of the radio and some of the optical sources are complex. Thus, it seems prudent to catalog IDs out to offsets of at least $1''$. In the few cases in which sources appear much more extended than the beam, an attempt has been made to assign an obvious ID. However, it is difficult to assess the reality of these IDs statistically.

In Figure 2 we show the histogram of optical magnitudes at R (within a $2''$ radius aperture) for the identifications. The mean magnitude for the 257 objects with identifications in the R -band image is 22.6. The median magnitude is about 23.0 with some uncertainty due to the sources confused by very bright objects and objects not detected in R because of image imperfections.

In order to estimate the reliability of the IDs, SExtractor was run on the central $8' \times 8'$ field of our R image, using an aperture of $2''$ radius. Since this field contains the central concentration of the cluster, the local source density should be somewhat higher than in the outlying fields. At a limiting magnitude of $R = 27.0$ (at which we begin to be incomplete), we find

0.01 objects per square arcsecond between 20.0 and 27.0 mag. Down to a brighter limit of $R = 25.0$, we find 0.0016 objects per square degree. Given our 329 unconfused objects, we expect 10 false identifications down to 27.0 mag. However, 77% of the objects have identifications brighter than 25.0. Since any objects fainter than 25.0 would be too faint to be designated the identification in the presence of a much brighter ID, we expect no more than one of these to be incorrect. Between 25.0 and 27.0 mag we might expect one false ID. Neither of these arguments takes into account the full effect of the brighter identifications, and thus this estimate is probably pessimistic. The argument does say that we expect a small number of cases in which the correct identification will have a fainter confusing source within the $1''$ search area (and the seeing disk) as well.

4. CONCLUSION

We have presented the data reduction techniques and the catalog of radio detections of non-cluster members for the A2125 field. We also report the R -band optical identifications. We report the catalog of the detections for confirmed cluster members in a companion paper, as well as a more detailed interpretation of these results. Subsequent papers will report more detailed astrophysical results for this data set.

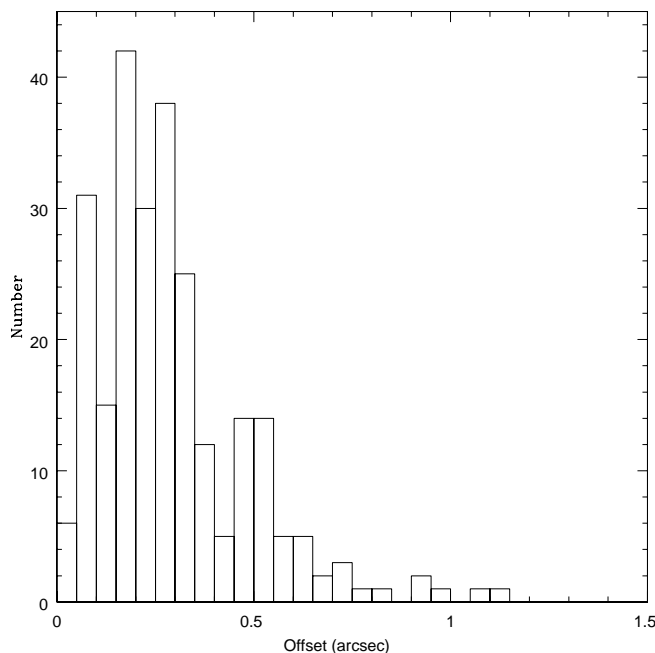


FIG. 1.—Histogram of the offsets between the positions of the radio sources and their optical identifications in arcseconds.

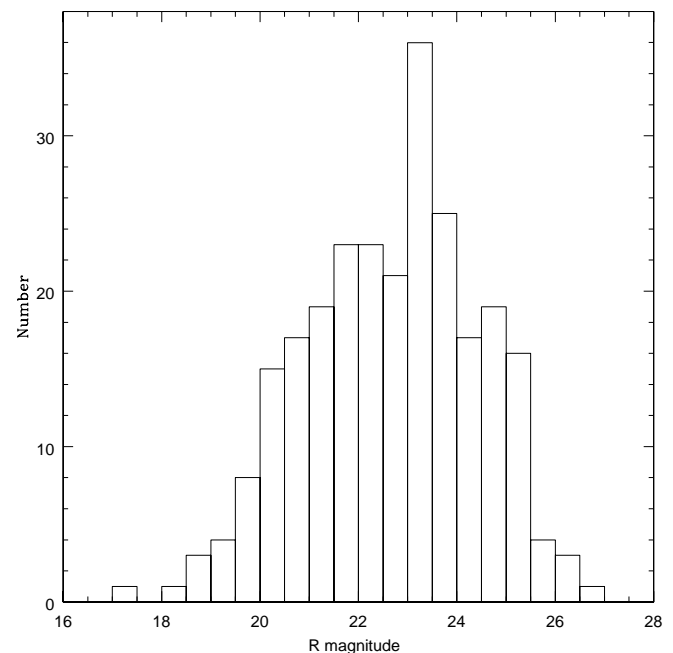


FIG. 2.—Histogram of R magnitudes of identifications in an aperture of $2''$ radius.

REFERENCES

- Carilli, C. L., & Yun, M. S. 1999, *ApJ*, 513, L13
- Condon, J. J. 1992, *ARA&A*, 30, 575
- Condon, J. J., Cotton, W. D., Greisen, E. W., Yin, Q. F., Perley, R. A., Taylor, G. B., & Broderick, J. J. 1998, *AJ*, 115, 1693
- Dwarakanath, K. S., & Owen, F. N. 1999, *AJ*, 118, 625
- Eales, S., Bertoldi, F., Ivison, R., Carilli, C., Dunne, L., & Owen, F. 2003, *MNRAS*, 344, 169
- Fan, X., et al. 1996, *AJ*, 112, 628
- Landolt, A. U. 1992, *AJ*, 104, 340
- Ledlow, M. J., Smail, I., Owen, F. N., Keel, W. C., Ivison, R. J., & Morrison, G. E. 2002, *ApJ*, 577, L79
- Miller, N. A., Owen, F. N., Hill, J. M., Keel, W. C., Ledlow, M. J., & Oegerle, W. R. 2004, *ApJ*, 613, 841
- Owen, F. N., Dyer, K., Ledlow, M. J., Keel, W. C., & Wang, Q. D. 2005a, in preparation
- Owen, F. N., Ledlow, M. J., Keel, W. C., & Morrison, G. E. 1999, *AJ*, 118, 633
- Owen, F. N., Ledlow, M. J., Keel, W. C., Wang, Q. D., & Morrison, G. E. 2005b, *AJ*, 129, 31 (Paper II)
- Valdes, F. G. 2002, in *Automated Data Analysis in Astronomy*, ed. R. Gupta, H. P. Singh, & C. A. L. Bailer-Jones (New Delhi: Narosa) (<http://iraf.noao.edu/projects/ccdmosaic/>)
- Wang, Q. D., Connolly, A., & Brunner, R. J. 1997, *ApJ*, 487, L13
- Wang, Q. D., Owen, F. N., & Ledlow, M. J. 2004, *ApJ*, 611, 821
- Xia, L., et al. 2002, *PASP*, 114, 1349
- Yun, M. S., Reddy, N. A., & Condon, J. J. 2001, *ApJ*, 554, 803